Collapse reliability of wind-excited reinforced concrete structures by stratified sampling and nonlinear dynamic analysis

Liuyun Xu[a], Seymour M.J. Spence[a,*]

[a]*Department of Civil and Environmental Engineering, University of Michigan, Ann Arbor, MI 48109, USA*

Abstract

Performance-based wind engineering (PBWE) is gaining consensus as an alternative to current wind design procedures for its potential to allow the explicit evaluation of system performance over a full range of performance objectives including collapse. To achieve the maximum benefits from PBWE, advanced computational approaches that enable the efficient prediction of the inelastic performance, as well as probabilities of failure under extreme winds, are essential. In this paper, a stochastic simulation-based framework is proposed to efficiently estimate the reliabilities/probabilities of failure of reinforced concrete (RC) structures subject to a full range of wind intensities. The framework is based on integrating a high-fidelity nonlinear modeling environment with a wind-tunnel-informed stochastic wind load model. An optimal stratified sampling scheme is adopted to propagate structural and load uncertainties and subsequently estimate the small probabilities of failure characterizing collapse with limited computational efforts. Through the illustration on a 45-story archetype RC building with a hypothetical location in New York City, the inelastic behavior and the subsequent reliabilities associated with various collapse limit states of interest are investigated. In particular, typical collapse mechanisms for the RC structures under extreme winds are explicitly captured by evaluating the progression of the localized damage, including reinforcing bar yielding, fracture, low-cycle fatigue failure, and concrete crushing.

Keywords: Performance-based wind engineering, Collapse reliability, Nonlinear dynamic analysis, Stochastic simulation

*Corresponding author

Email addresses: xliuyun@umich.edu (Liuyun Xu), smjs@umich.edu (Seymour M.J. Spence)

1. Introduction

Current wind practice consists in designing the structural system through linear elastic analysis under a limited set of wind loads corresponding to specific hazard levels identified from climatological studies [1]. Consequently, the system-level post-yield wind performance is not explicitly evaluated. Nevertheless, extreme wind hazards can cause irreversible structural and/or nonstructural damage that can only be mitigated by considering an appropriate suite of explicit system-level inelastic limit states that ensure structural safety against potential collapse. To this end, performance-based wind engineering (PBWE) has been proposed as a fundamental shift to current practice in wind engineering [2, 3, 4, 5, 6, 7, 8], that places focus on comprehensively evaluating the system-level structural performance at various wind intensities, including those that can cause collapse.

A core objective of state-of-the-art PBWE is to predict the inelastic performance and the reliabilities of structures subject to wind events beyond those prescribed in current codes for design. While the accumulated knowledge related to the dynamic nonlinear response modeling in performance-based earthquake engineering (PBEE) [9, 10] is useful and instructive for developing PBWE guidelines, several challenges exist in developing a robust framework for predicting the inelastic behavior up to collapse of wind-excited structural systems. These include [1]: 1) the long duration (in the order of hours) of typical dynamic wind loads which create a significant computational barrier to propagating uncertainty and therefore estimating probabilistic performance metrics; and 2) the complexity of modeling nonlinear wind responses where the presence of a substantial mean wind load component (for certain wind directions) can create theoretical difficulties in applying state-of-the-art modeling schemes developed for PBEE. However, to fulfill the maximum potential of PBWE, advanced computational frameworks that enable the probabilistic prediction of the inelastic and collapse performance of wind-excited structural system through nonlinear analysis are indispensable [11, 1]. Considerable research efforts have been placed on developing advanced approaches for predicting nonlinear wind response with uncertainty propagation. For example, Judd and Charney [12] investigated the nonlinear dynamic response and risk of collapse of single-degree-of-freedom (SDOF) multistory building models, Feng and Chen [13, 14] introduced two statistical linearization approaches for modeling the inelastic along-wind as well as the

across-wind response of wind-excited tall buildings, while Huang and Chen [15] quantified the uncertainty associated with using reduced order models. Chuang and Spence [16, 17, 18, 19] proposed a probabilistic performance assessment framework for evaluating the reliabilities of wind-excited steel structures through the application of dynamic shakedown while considering a full range of load and model uncertainties that are consistent with those considered in developing current codes and standards. Arunachalam and Spence [20] developed a similar framework while, however, considering high-fidelity nonlinear modeling and increased resolution in the description of the model uncertainties. Zheng et al. [21] presented a hybrid Bayesian-Copula-based method for assessing the wind-induced risk of tall buildings subject to aleatory and epistemic uncertainties. On the other hand, extensive studies have focused on developing data-driven methodologies for predicting system response under uncertainty and subsequently estimating reliabilities. Their efficiency in wind engineering applications has been demonstrated [24, 22, 23]. Their efficiency in wind engineering applications has been widely demonstrated [22, 23, 24]. Regardless of these and other efforts devoted to probabilistic performance assessment of wind-excited structures, there is not yet a consensus on approaches for estimating inelastic performance, including collapse, while treating the estimation of the small failure probabilities generally associated with inelastic limit states. In addition, notwithstanding how reinforced concrete (RC) is perhaps the most widely adopted material in developing the structural systems of wind-excited high-rise buildings, the high-fidelity modeling of RC structural systems within a PBWE setting has received little attention. This is most likely due to the strong nonlinearity associated with concrete materials which directly increases the difficulty of modeling and predicting the inelastic behavior of RC systems.

In response to the aforementioned needs, this work is focused on developing an efficient simulation framework for investigating the reliabilities as well as the inelastic/collapse behavior of high-rise RC structural systems subject to extreme stochastic dynamic wind loads and general model uncertainties. To this end, high-fidelity finite element models are developed to directly capture the inelastic behavior of RC structural systems subject to a full range of wind intensities. A stratified sampling scheme is introduced to propagate general uncertainties and enable the direct estimation of the small probabilities of failure associated with

rare events such as collapse. The proposed framework is illustrated on a 45-story archetype RC building with a hypothetical location in New York City. Reliabilities (or failure probabilities) associated with various inelastic limit states of interest are investigated. To identify the collapse mechanism of high-rise RC buildings, the progression of inelasticity as well as localized damage (e.g., reinforcing bar buckling, fracture, fatigue, and concrete crushing) is explicitly evaluated.

2. Framework Outline

2.1. Reliability Problem

Advanced PBWE aims to describe performance in terms of probabilistic metrics estimated from solving a system-level reliability problem based on the inelastic behavior of the structural system. Essential to this performance evaluation is the identification of an adequate set of random variables that account for the uncertainties in the wind hazard, the stochastic nature of the dynamic wind loads (record-to-record variability), and the uncertainties in the model parameters (e.g., mechanical parameters and component capacities). For describing the intensity of the wind hazard while accounting for wind direction effects, a variety of approaches have been developed [25]. In this work, the practical and commonly adopted sector-by-sector approach is adopted in which wind direction is divided into N_{sec} equal-sized sectors [26, 25]. Given a limit state of interest, R, the probability of failure is therefore defined as:

$$P_{f_R} = \max_{1 \leq n \leq N_{\text{sec}}} \left[P_{f_R}^{(n)} \right] \tag{1}$$

where $P_{f_R}^{(n)}$ is the failure probability in sector n. To estimate $P_{f_R}^{(n)}$, the following equation requires solving:

$$P_{f_R}^{(n)} = P(g_R \leq 0) = \iint G(g_R \leq 0 | \alpha, \bar{v}_H) | dG_n(\alpha | v_H) | | dG_n(v_H) | \tag{2}$$

where g_R is the limit state function associated with R that assumes negative values upon exceedance of R; $G_n(v_H)$ represents the site-specific complementary cumulative distribution function (CCDF) of the maximum mean hourly wind speed, v_H, to occur over the lifespan of the structure (e.g., 50 years) in sector n; $G_n(\alpha | v_H)$ is the CCDF governing wind direction conditional on v_H in sector n; while $G(g_R | \alpha, \bar{v}_H)$ is the CCDF of failure ($g_R \leq 0$) conditional

on an event of wind speed, $\bar{v}_H$, and wind direction, α. Inherent to $G(g_R|\alpha, \bar{v}_H)$ are the effects of the uncertainties in the dynamic wind loads (i.e., the stochasticity of the dynamic wind records) as well as the model parameters (i.e., uncertainty in component capacities, mechanical parameters, etc.). In particular, to estimate $G(g_R|\alpha, \bar{v}_H)$ for limit states that involve inelasticity, nonlinear dynamic analysis is necessary. It should also be observed that the estimation of $G_n(v_H)$ requires a certain amount of engineering judgment, especially if the partial correlation between the sectorial wind speeds is to be captured.

Given P_{f_R} from Eq. (1), the associated reliability index, β_R, can be estimated as:

$$\beta_R = \Phi^{-1}(1 - P_{f_R}) \tag{3}$$

where Φ is the standard normal cumulative distribution function.

2.2. Response Analysis

To estimate the probability of failure of Eq. (2), the term $G(g_R \leq 0|\alpha, \bar{v}_H)$ requires the prediction of the inelastic response of the structural system subject to a vector of stochastic dynamic wind loads and characterized by general model uncertainty. This can be achieved by solving the following equations of motion:

$$\boldsymbol{M}(\boldsymbol{y}_m)\ddot{\boldsymbol{u}}(t) + \boldsymbol{f}_D(\boldsymbol{u}(t), \dot{\boldsymbol{u}}(t), \boldsymbol{y}_m) + \boldsymbol{f}_r(\boldsymbol{u}(t), \boldsymbol{y}_m) = \boldsymbol{f}(t; v_H, \alpha, \boldsymbol{y}_h) \tag{4}$$

where, $\ddot{\boldsymbol{u}}(t)$, $\dot{\boldsymbol{u}}(t)$ $\boldsymbol{u}(t)$ are the displacement, velocity, acceleration response vectors of the system; $\boldsymbol{f}(t; v_H, \alpha, \boldsymbol{y}_h)$ is the stochastic dynamic wind load for a given wind speed, v_H, and wind direction, α; $\boldsymbol{y}_h$ is a random vector characterizing the uncertainty in the wind hazard model (including the stochasticity of the dynamic wind loads); $\boldsymbol{M}$ is the mass matrix; $\boldsymbol{y}_m$ is a random vector characterizing the uncertainty in the structural model (e.g., parameters of the material constitutive laws and geometric uncertainties); while $\boldsymbol{f}_D$ and $\boldsymbol{f}_r$ are the nonlinear damping and restoring forces that are generally dependent on response of the system and encapsulate both material and geometric uncertainty.

In general, given a realization of $\boldsymbol{f}(t)$ and $\boldsymbol{y}_m$, to solve Eq. (4) direct time integration schemes are required. Because of their efficiency, implicit schemes are a popular choice, for example, the well-established class of Newmark-beta algorithms. However, as also observed in [27], for highly nonlinear problems, e.g., collapse simulation, implicit schemes can have

significant convergence issues. This is especially true for RC structures as concrete has a highly nonlinear constitutive law even at relatively small deformations (i.e., unlike steel, it is not characterized by an essentially elastic region before yielding). To overcome this, explicit schemes (i.e., central difference, leap-frog, etc.) are more suitable notwithstanding their increased computational effort, as compared to implicit schemes, due to the need to consider time steps that are related to the highest natural frequency of the system.

In addition, before solving Eq. (4), gravity loads must be applied and the static system response estimated. In other words, Eq. (4) is solved at the end of a static load step involving the application of a vector of gravity loads, $\boldsymbol{f}_g$, related to both dead loads and vertical live loads. In particular, $\boldsymbol{f}_g$ is also uncertain while the response of the system due to $\boldsymbol{f}_g$ depends on the model uncertainties $\boldsymbol{y}_m$. Therefore, before solving Eq. (4), the uncertainty in $\boldsymbol{f}_g$ requires characterization which also involves identifying appropriate vertical live loads for combination with the stochastic dynamic wind loads $\boldsymbol{f}(t)$.

2.3. Limit State Functions

As outlined in Sec. 2.1, this work is focused on estimating the probability of failure of the system through solving Eq. (2) for any given limit state, R, of interest. Given R, this involves defining the following limit state function:

$$g_R = R - D(\ddot{\boldsymbol{u}}(t), \dot{\boldsymbol{u}}(t), \boldsymbol{u}(t)) \tag{5}$$

where D is an operator extracting from the dynamic response of the system the demand parameter to compare against R. To allow for the consideration of a general class of limit states related to the performance of RC structural systems under extreme winds, no limitations on the definition of D or R are imposed therefore allowing for the inclusion of both system and component level limit states, including limit states in which R presents significant uncertainty. In particular, the system-level limit states that will be considered are related to excessive inelastic deformation, in terms of both peak inter-story and residual drift ratios, that can lead to collapse, while the component-level limit states are related to concrete crushing, reinforcing bar buckling and fracture.

3. Background Structural and Wind Load Models

3.1. Fiber-based Modeling of RC Structural Systems

RC systems of high-rise buildings often involve shear walls and/or core systems together with beams (including coupling beams) and columns. While the finite element modeling of the beams and columns of such systems can be carried out using common nonlinear fiber-based beam-column elements (e.g., the displacement-/force-based beam-column elements of OpenSees [28]), such an approach is limited in the modeling of shear walls and/or cores by the need to embed auxiliary beam-column/link elements for capturing the three-dimensional interaction of such systems in resisting lateral loads. This directly influences the accuracy/validity of the nonlinear structural analysis [29, 30]. To overcome the aforementioned limitation, the OpenSees modeling environment is adopted in this work with wall/core systems modeled using the three-dimensional four-node Multiple-Vertical-Line-Element-Model-3D (MVLEM-3D) element that was specifically developed for the nonlinear analysis of flexure-controlled non-rectangular reinforced concrete walls subjected to multidirectional loading [30, 31]. The MVLEM-3D element is founded on a discretization based on macro fibers that avoids the use of additional embedded elements and enables the simulation of distributed plasticity along the length, width, and depth of the element. Out-of-plane behavior is described by a four-node Kirchhoff plate model while in-plane shear is modeled by an uncoupled linear or nonlinear shear spring. The element allows the consideration of both confined and unconfined concrete in defining the macro fibers. Validated by comprehensive quasi-static experiments, the MVLEM-3D element is well suited for the modeling of three-dimensional RC structures and represents a good balance between efficiency and accuracy [30]. Because the framework of this work is developed using OpenSees as the finite element modeling environment, if deemed necessary, more sophisticated finite elements can be considered, including the three-dimensional Shear-Flexure Interaction Multiple-Vertical-Line-Element-Model (SFI-MVLEM-3D) that explicitly captures axial-flexural and shear interaction [32].

To capture the effects of large rotations and displacements in a small deformation/strain setting, a corotational formulation [33] is implemented in this work. The basic reference system of the individual finite elements is therefore considered fixed to the element as it

deforms while the rotation and translation of this reference system is described through rigid body motions.

3.2. Material and Damping Models

3.2.1. Concrete and Reinforcing Steel Material Models

Essential to a reliable prediction of the nonlinear behavior of RC structures are adequate hysteretic models for describing the fiber-level stress-strain relationship in both cyclic compression and tension for both the concrete and reinforcing materials [34].

For concrete, the uniaxial constitutive stress-strain relationship for cyclic loading suggested in Yassin [35] offers a good balance between accuracy and efficiency. In this model, the monotonic stress-strain curves for concrete in compression follow the relationship suggested by Kent and Park [36] and Scott et al. [37], while the hysteretic unloading and reloading curves are a set of linear stress-strain relationships. It should be noted that in its classic form, this model continues with a non-zero stress level after crushing. To directly capture the concrete crushing phenomenon, each concrete fiber can be wrapped in a MinMax material model which drops the stress and stiffness to zero upon the first occurrence of a predefined strain limit. This approach is followed in this work.

For modeling the hysteretic behavior of the reinforcing steel, the well-known Menegotto-Pinto material model [38], with the extensions outlined in Filippou et al. [39] to include isotropic strain hardening effects, is adopted. This model is formed by two straight-line asymptotes, with slopes E_0 (elastic modulus) and E_1 (yield modulus), for defining the elastic and post-yield behavior of the reinforcing steel. A curved transition is incorporated between the two asymptotes, permitting the Bauschinger effect to be represented. The curvature of the transition curve is controlled by a parameter that depends on the difference in absolute strain between the current asymptote intersection point and the previous maximum (or minimum) strain reversal point. This parameter can be degraded, as in this work, for strain reversals in both pre- and post-yielding regions therefore providing a more accurate prediction of the member capacity. To capture reinforcing fracture and buckling failure, each steel fiber can be wrapped in a MinMax material which drops the stress and stiffness to zero upon reaching predefined tensile and compressive strain limits at which fracture in tension and buckling in

compression is expected. Additionally, due to the long duration of typical wind events (in the order of hours), a low cycle fatigue (LCF) material model capable of capturing reinforcing bar failure due to damage accumulation is essential. In this work, an approach is adopted based on the classic Coffin-Manson relationship for which the total strain amplitude, ϵ_i, is assumed to be related to the number of constant cycles to failure, N_f, through the expression [40, 41]:

$$\epsilon_i = \epsilon_0 (N_f)^m \tag{6}$$

where ϵ_0 indicates the strain amplitude at which fracture will occur due to a single complete cycle; m defines the slope of the Coffin-Manson curve in the log-log space, which describes the sensitivity of the log of ϵ_i to the log of N_f. To estimate the accumulation of damage for a fiber subject to varying amplitude cycles, the modified rainflow cycle counting method outlined in Uriz [40] is adopted. The approach is based on defining the damage index, DI_i, for a given amplitude, ϵ_i, as the ratio of the number of cycles, n_i, and the number of constant amplitude cycles, N_{fi}, necessary to cause failure at ϵ_i. Subsequently, the overall damage is estimated as the sum of damage occurring at all amplitudes:

$$DI = \sum \frac{n_i}{N_{fi}} \tag{7}$$

Once DI reaches unity, reinforcing bar fracture due to LCF failure occurs and the fiber stress and stiffness is dropped to zero. Importantly, the modified cycle counting method is based on counting half cycles and therefore encompasses failure due to monotonic strain increases typical of along-wind type of wind loading.

3.2.2. Damping Model

A classic approach for defining the damping force, $\mathbf{f}_D$, is the adoption of a Rayleigh damping model which, for nonlinear systems, can be written in the following form [42]:

$$\mathbf{f}_D(\dot{\mathbf{u}}(t), \mathbf{u}(t)) = (c_0 \mathbf{M} + c_1 \mathbf{K}_t)\dot{\mathbf{u}}(t) = \mathbf{C}_t \dot{\mathbf{u}}(t) \tag{8}$$

where c_0 and c_1 are the Rayleigh proportionality coefficients estimated from the initial stiffness matrix of the system, $\mathbf{K}_t$ is the tangent stiffness matrix computed at the end of the previous time step (last-committed state) during nonlinear dynamic analysis, and $\mathbf{C}_t = c_0\mathbf{M} + c_1\mathbf{K}_t$

which represents the current damping matrix. While the adoption of the classic Rayleigh damping model of Eq. (8) can be considered together with explicit time integration schemes, it is not recommended as the non-diagonal nature of $\mathbf{C}_t$ precludes the use of diagonal solvers for the resolution of the system of equations at each time step. This can significantly decreases computational efficiency, especially for large scale systems such as those considered in this work [27]. As an alternative, the damping matrix can be constructed by the superposition of modal damping matrices specified for a set of modes of interest [43]. However, unless all modes are considered (which for large scale finite element systems is complex due to numerical issues in identifying the higher modes), this model assumes zero damping in the higher modes, and therefore often leads to local response (e.g., fiber level response) oscillations. These difficulties can be solved through considering a mass proportional damping matrix, i.e., $\mathbf{C}_t = c_0\mathbf{M}$, which can be calibrated by specifying the damping ratio for the first natural frequency of the system estimated from the initial stiffness matrix. This approach ensures a diagonal damping matrix as well as damping in all the vibration modes of the system therefore eliminating spurious oscillations in the local responses. In general, mass proportional damping will underestimate overall damping therefore ensuring a conservative estimate of the resulting response. It should be observed that for highly nonlinear systems, such as those considered in this work, a significant proportion of damping will come from the hysteretic response of the system which is not affected by the choice of damping model.

3.3. Stochastic Wind Load Model

The path-dependent nature of the nonlinear dynamic analysis implies the need to define appropriate initial and final conditions for the dynamic wind load history, $\mathbf{f}(t)$. This can be achieved by defining $\mathbf{f}(t)$ through the use of an appropriate envelope function, $e(t)$, and therefore as:

$$\mathbf{f}(t; v_H, \alpha, \boldsymbol{y}_h) = e(t)\tilde{\mathbf{f}}(t; v_H, \alpha, \boldsymbol{y}_h) \tag{9}$$

where $\tilde{\mathbf{f}}(t)$ is the stationary representation of $\mathbf{f}(t)$. As suggested in Judd and Charney [12], Judd [44], Chuang and Spence [18, 19], it is common in wind engineering to assume $e(t)$ so as

to linearly ramp the initial/final part of $\tilde{\mathbf{f}}(t)$. This leads to the following envelope function:

$$e(t) = \begin{cases} t/T_a, & t \in [0, T_a) \\ 1, & t \in [T_a, T_b) \\ 1 - (t - T_b)/(T - T_b), & t \in (T_b, T] \end{cases} \tag{10}$$

where, T_a is the length of the initial linear ramp, T_b is time at which the final linear ramp starts while T is the total duration of $\tilde{\mathbf{f}}(t)$.

To characterize the stationary vector $\tilde{\mathbf{f}}(t)$ a model capable of capturing the complex aerodynamic features characteristic of high-rise buildings (i.e., vortex shedding, detached flow and interference effects from surrounding buildings) is required, as is a model that can capture the record-to-record variability/stochasticity associated with dynamic wind loads. To achieve this, the data-driven proper orthogonal decomposition (POD)-based spectral representation model outlined in [45, 46, 47] is adopted in this work. The jth component of $\tilde{\mathbf{f}}(t)$ is therefore written as:

$$\tilde{f}_j(t; v_H, \alpha, \boldsymbol{y}_h) = w_1 w_2 w_3 \sum_{l=1}^{N_l} \sum_{n_1=0}^{N_\omega - 1} 2|\Psi_{jl}(\omega_{n_1}; \alpha)| \sqrt{\Lambda_l(\omega_{n_1}; v_H, \alpha) \Delta\omega} \cos(\omega_{n_1} t + \vartheta_{jl}(\omega_{n_1}; \alpha) + \theta_{n_1 l}) \tag{11}$$

where, N_l is the total number of spectral POD modes considered in the expansion; N_ω is the total number of discrete frequencies; $\Delta\omega$ is the frequency increment with $\omega_{n_1} = n_1 \Delta\omega$; $\theta_{n_1 l}$ is a uniformly distributed basic random variable in $[0, 2\pi]$ generating the stochasticity in the dynamic wind loads; $\vartheta_{jl} = \tan^{-1}(\mathrm{Im}(\Psi_{jl})/\mathrm{Re}(\Psi_{jl}))$; $\Psi_{jl}(\omega)$ is the jth component of the lth wind tunnel data estimated spectral POD eigenvector; $\Lambda_l(\omega)$ is the lth wind tunnel data estimated eigenvalue; and w_1, w_2, and w_3 are random variables that account for the uncertainties associated with the sampling errors due to the finite length of the wind tunnel record, the use of scaled models, and observational errors when estimating $\Psi_l(\omega)$ and $\Lambda_l(\omega)$ from wind tunnel records.

The fundamental characteristic of the stochastic wind load model of Eq. (11) is the calibration of $\Psi_l(\omega)$ and $\Lambda_l(\omega)$ to building specific wind tunnel data. This ensures the model is capable of capturing all the aerodynamic features seen in the wind tunnel.

4. Structural Model and Load Uncertainties

4.1. Preamble

A comprehensive description of the uncertainties affecting the system is essential for a meaningful estimation of the failure probability of Eq. (2). This involves defining the parameters of the random vectors $\boldsymbol{y}_m$ and $\boldsymbol{y}_h$, which complement the wind intensity measures v_H and α, so has to adequately describe all important sources of uncertainty therefore ensuring the estimated failure probabilities (or reliabilities) are of use to the decision making process, for example, they can be compared to the target reliabilities at the core of many modern codes and standards (e.g., Table 1.3-1 of ASCE 7-22 [48]). Before proceeding, it is important to observe that the random vector $\boldsymbol{y}_m$ is non-ergodic in time (i.e., its statistical properties cannot be obtained by temporal averaging), whereas $\boldsymbol{y}_h$ is ergodic. As illustrated in Kiureghian [49] for seismic applications, this can lead to errors in the failure probabilities estimated from Eq. (2). Nevertheless, for small lifetime failure probabilities, i.e., less than 0.01 for the seismic applications outlined in Kiureghian [49] over lifespans of 50 years, these errors are negligible. Because this paper is focused on collapse probabilities that are expected to be in the order of 10^{-5} to 10^{-7} over lifespans of 50 years, the distinction between ergodic and non-ergodic random variables is neglected as this assumption provides significant computational advantages (i.e., ergodic and non-ergodic random variables can be simultaneously sampled). Having said this, it is important to observe that wind excitation is generally significantly longer than seismic excitation. This could lead to increased errors associated with the neglect of the difference between ergodic and non-ergodic random variables and should constitute a topic of future investigation.

4.2. Structural Model Uncertainties

4.2.1. Concrete Material Uncertainty

The modeling approach of this work is based on fiber discretizations. The mechanical properties of the materials are therefore defined at the level of the material constitutive laws. As discussed in Sec. 3.2.1, the constitutive law for confined and unconfined concrete is modeled in this work by adopting the modified Kent and Park model outlined in Scott

et al. [37], Yassin [35], Orakcal [34], although any other model could be adopted without compromising the proposed framework.

As illustrated in Fig. 1, the skeleton curve of this model is defined by the following parameters: compressive strength of the concrete at 28 days, f'_c; concrete strain at maximum strength, ϵ_0; the factor K modeling the strength increase due to confinement; and the strain softening slope Z. In particular, the strain at maximum strength can be estimated as $\epsilon_0 = 0.002K$ while ϵ_{20} is estimated from the intersection of the strain softening portion of the envelope curve and the point of 20% maximum strength, $0.2Kf'_c$. The parameters governing the skeleton curve in tension, i.e., f_t and E_t, can be derived directly from f'_c and ϵ_0 [30]. The degradation of stiffness during cyclic unloading and reloading is governed by the parameter λ.

In terms of uncertainties, f'_c can be treated as a lognormal basic random variable with mean related to the nominal compressive strength through the factors outlined in [50] and coefficient of variation (COV) of 0.2 [51, 52]. The parameters Z, K, f_t, and E_t, on the other hand, can be treated as derived random variables. In particular, following the expressions outlined in Yassin [35], Z depends on f'_c as well as the yield strength of the transverse reinforcement, f_{yh}, whose randomness can be characterized as described for the longitudinal reinforcement of Sec. 4.2.2, and the ratio of the volume of transverse reinforcement to the volume of concrete core, ρ_s, which is random due to the geometric uncertainties of Sec. 4.2.3. Likewise, in terms of random parameters, Z depends on f'_c, f_{yh}, and ρ_s as well as the width of the concrete core to the outside of the stirrups, h', which is random due to the geometric uncertainties of Sec. 4.2.3. From the expressions for f_t and E_t suggested in [30], the uncertainty in f_t and E_t can be fully characterized from the knowledge f'_c and K. Due to an absence of information for uncertainty characterization, λ is generally taken as deterministic.

4.2.2. Steel Material Uncertainty

As discussed in Sec. 3.2.1, the extended Menegotto-Pinto constitutive law was considered in this work for characterizing the mechanical response of the steel fibers of the reinforcement. Of the parameters defining this model, there is adequate information available in the literature

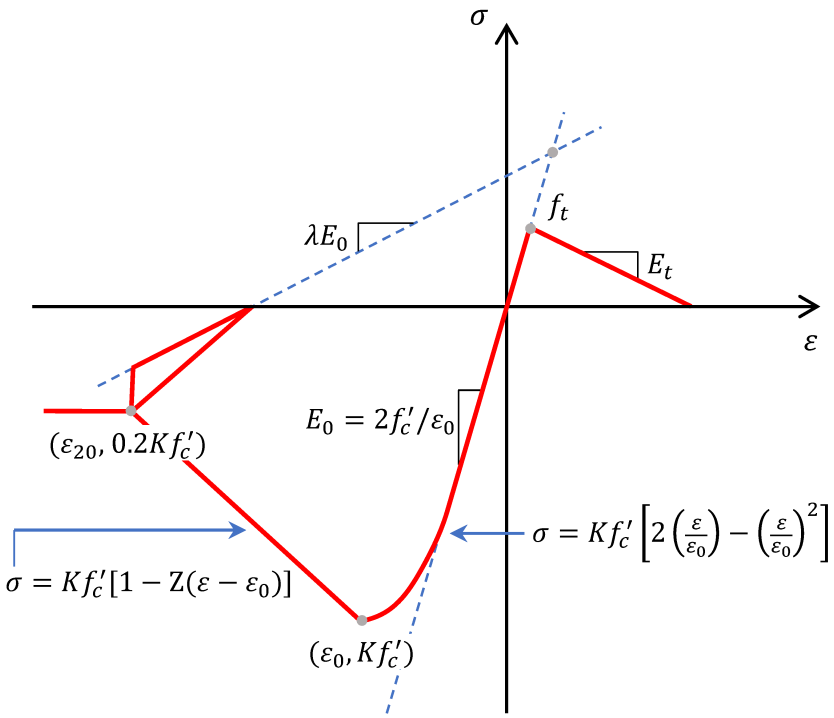

Figure 1: Concrete material parameters.

to model the yield stress, F_y (f_{yh} for transverse reinforcement), initial tangent modulus, E_0, and the strain hardening ratio, b, as basic random variables with the distributions reported in Table 1. These parameters will in general present a certain degree of probabilistic dependency that can be modeled through assigning a correlation structure which, however, will be based primarily on engineering judgment due to a lack of available data [53, 52]. Similarly, due to an absence of information for uncertainty characterization, the model parameters governing the initial and degraded curvature of the constitutive law are generally treated as deterministic as are the parameters governing the isotropic hardening in tension and compression.

To model the uncertainty in the occurrence of fracture of the reinforcing bars, the strain at which fracture is expected to occur, ϵ_{sh}, can be treated as a random variable with distribution as reported in Table 1. To model the uncertainty in the buckling of the reinforcing bars, it is suggested in this work to relate the buckling of the reinforcing bars to the crushing of the concrete. Therefore, reinforcing bars are considered to buckle with the crushing of the surrounding concrete which is governed by the randomness in ϵ_{20}, as characterized in Sec.

Table 1: Random variables of the steel constitutive law.

Parameter	Mean	COV	Distribution	Reference
F_y or f_{yh}	$1.1F_{yn}$ or $1.1f_{yhn}$	0.106	Beta	[51, 52, 20]
E_0	200Gpa	0.033	Lognormal	[51, 52, 20]
b	0.02	0.2	Lognormal	[51, 52, 20]
ϵ_0	0.077	0.161	Lognormal	[20, 54]
ϵ_{sh}	0.1	0.00133	Lognormal	[52, 54, 55]

F_{yn} or f_{yhn}: Nominal yield strength of the reinforcing bars

4.2.1. With respect to LCF, to model the uncertainty in fatigue failure of the reinforcing bars the strain amplitude at which failure will occur due to a single complete cycle, ϵ_0, can be modeled as a basic random variable with the distribution reported in Table 1.

4.2.3. Geometric Uncertainty

Uncertainties in the geometric properties of the components, e.g., cross-sectional dimensions, thickness of concrete cover, and cross-sectional area of the reinforcing bars, are small but not negligible [52]. Within the fiber-based modeling environment outlined in Sec. 3.1, the geometric parameters that can be modeled as uncertain depend on the finite element type used to model the component. For components schematized using fiber-based beam-column elements, uncertainty can be considered in the width, b_c, depth, h_c, and concrete cover thickness, t_s, as well as the cross-sectional area of the longitudinal reinforcing steel, A_s. For components schematized using fiber-based MVLEM-3D elements, the thickness of the element, b_s, can be taken as uncertain while the uncertainty in the cross-sectional area of the longitudinal reinforcing steel can be indirectly modeled through the reinforcing ratio: $\rho_{sv} = A_s/A_{\text{gross}}$ where A_{gross} is the gross area of the element (also random due to the uncertainty in b_s). In addition to the above parameters and consistently with assuming A_s as uncertain, the area of the transverse reinforcement, A_{sh}, can also be taken as uncertain. This will affect the concrete constitutive law of Sec. 4.2.1 through ρ_s and therefore the volume of transverse reinforcement to the volume of the concrete core of the component.

Table 2: Geometric Uncertainties.

Parameter	Mean	COV	Distribution	Reference
b_c	nominal	0.055	Normal	[52]
h_c	nominal	0.055	Normal	[52]
t_s	75 mm	0.1	Normal	[53]
b_s	nominal	0.055	Lognormal	[52]
A_s or A_{sh}	nominal	0.02	Normal	[53]

Appropriate distributions for the geometric parameters b_c, h_c, t_s, b_s, A_s, and A_{sh} can be found in the literature as reported in Table 2.

4.2.4. System Uncertainties

Together with the uncertainties at the local material level, characterization of uncertainty at the level of the entire system is also required. This includes defining appropriate models for characterizing the uncertainty in the damping model of Sec. 3.2.2 which, due to the assumption of a Rayleigh model, requires the characterization of the first two modal damping ratios, $\boldsymbol{\zeta} = \{\zeta_1, \zeta_2\}^T$ (this reduces to the first modal damping ratio in the case mass proportional damping is adopted). The most straightforward approach to modeling this uncertainty is to treat $\boldsymbol{\zeta}$ as a basic random vector with fully correlated components that follow a lognormal distribution with mean 0.02 and COV 0.2 [52]. The parameters of the Rayleigh model, c_0 and c_1 of Eq. (8), can then be treated as derived random variables defined by calibrating the initial damping matrix to the components of $\boldsymbol{\zeta}$ at the first two natural frequencies of the system estimated from the initial tangent stiffness (also uncertain due to the randomness in the material constitutive laws) and current mass matrix (uncertain due to the randomness in the dead loads).

An additional source of system uncertainty that requires characterizing is the probabilistic dependence between the parameters of the constitutive laws of different components. With respect to the basic random variables of the concrete constitutive law, for multi-story buildings, these will present significant correlations over each floor level as concrete is generally

poured floor-by-floor. The basic random variables of the constitutive law of the steel reinforcing will also present a significant correlation for reinforcing cages made from the same steel batch. However, multiple steel batches will in general be required in the construction of a multi-story building. Using engineering judgment, the basic random variables of the steel reinforcing constitutive law are also considered to vary from floor to floor. Therefore, in this work, each floor level is associated with a separate set of basic random variables modeling the uncertainty in the steel and concrete constitutive laws and collected in the vector $\boldsymbol{\kappa}_{c,j} = \{f'_c, F_y, f_{yh}, E_0, b, \epsilon_0, \epsilon_{sh}\}^T$ where j is the floor number.

In addition to the parameters of the constitutive laws, the geometric uncertainties can also present dependence between components. In this work, b_c, h_c, t_s, and b_s are considered independent basic random variables that vary between different components. Consistently with how the parameters of the constitutive law of the reinforcing steel are treated, A_s and A_{sh} are considered to vary floor by floor. The geometric uncertainties therefore define the following random vector $\boldsymbol{\kappa}_{g,j} = \{b_{c,1}..., b_{c,n_j}, h_{c,1}, ..., h_{c,n_j}, t_{t,1}..., t_{t,n_j}, b_{s,1}..., b_{s,k_j}, A_s, A_{sh}\}^T$ where n_j and k_j are respectively the number of components modeled as beam-column and MVLEM-3D elements at floor j.

The above random variables allows for the definition of the random vector of model uncertainties as: $\boldsymbol{y}_m = \{\boldsymbol{\zeta}^T, \boldsymbol{\kappa}^T_{c,1}, ..., \boldsymbol{\kappa}^T_{c,N_f}, \boldsymbol{\kappa}^T_{g,1}, ..., \boldsymbol{\kappa}^T_{g,N_f}\}^T$ where N_f is the total number of floors of the building under consideration.

4.3. Load Uncertainties

4.3.1. Wind Load Uncertainty

The uncertainty in the external dynamic loads, $\mathbf{f}(t)$, are arguably the most important source of uncertainty driving the reliability of the system. As discussed in Sec. 2.1, it is common to use v_H (maximum mean hourly wind speed) over the lifespan of the structure and α (associated wind direction) as random variables describing the intensity of the wind event. Additionally, the record-to-record variability (stochasticity) is another source of randomness that requires consideration in extreme response analysis due to the path-dependency of nonlinear analysis. This is captured in Eq. (11) for each POD mode through the independent and identically distributed sequences $\boldsymbol{\theta}_l = \{\theta_{1l}, \theta_{2l}, ..., \theta_{n_1 l}, ..., \theta_{N_\omega l}\}^T$. In addition,

Table 3: Random variables associated with experimental wind tunnel data.

Parameter	Mean	COV	Distribution	Reference
w_1	1.0	0.075	Truncated Normal	[56]
w_2	1.0	0.05	Truncated Normal	[57, 58]
w_3	1.0	0.05	Truncated Normal	[57, 58]

uncertainties associated with calibrating Eq. (11) to experimental wind tunnel data should be considered and are in the proposed framework through the random variables w_1, w_2, and w_3 of Sec. 3.3. In particular, appropriate distributions for w_1, w_2, and w_3 are reported in Table 3.

The above random variables allows for the definition the random vector of wind hazard uncertainties as: $\boldsymbol{y}_h = \{w_1, w_2, w_3, \boldsymbol{\theta}_1^T, ..., \boldsymbol{\theta}_{N_l}^T\}^T$.

4.3.2. Gravity Load Uncertainty

As discussed in Sec. 2.2, before solving Eq. (4), a vector of uncertain gravity loads, $\boldsymbol{f}_g$, must be applied to the system. In particular, together with the dead and super dead loads, D, appropriate "arbitrary point-in-time" live loads, L_{apt}, are required for combination with the external dynamic wind loads. Extensive literature exists on the probabilistic characterization of both D and L_{apt} whose values are generally related to the nominal values of D and L_{apt}, as outlined in Table 4. With respect to correlation, it is common to assume D and L_{apt} as independent random variables. Individually, D is generally assumed perfectly correlated at each floor level as is L_{apt} [59]. The application of D and L_{apt} to the structural model results in a system of nodal forces (derived from appropriate fixed end force relationships for distributed loads) that define the random vector $\boldsymbol{f}_g$. It should be observed that the randomness in the gravity loads will in general generate randomness in the mass matrix, $\boldsymbol{M}$, of the system.

Table 4: Characterization of the gravity load uncertainty.

Parameter	Mean	COV	Distribution	Reference
D	$1.05D_n$	0.1	Normal	[59, 60]
L_{apt}	$0.24L_{rn}$	0.6	Gamma	[59, 61]

D_n: Nominal dead load

L_{rn}: Nominal reduced live load

5. Stochastic Simulation Strategy

The major goal of this work is to efficiently estimate the failure probability (or reliability) of the system through solving Eq. (2) for a suite of limit states, including collapse, while considering the uncertainties introduced in Sec. 4 as well as the sectorial hazard intensity measures v_H and α. The significant computational burden of the nonlinear dynamic response analysis required for characterizing the failure of the systems of interest to this work implies the need to adopt variance reduction methods for assessing Eq. (2). This is especially true if it is recognized that probabilities associated with limit states such as collapse are extremely small (often in the order of 10^{-5} – 10^{-7} for well-designed systems). The need to simultaneously estimate the failure probability for multiple limit states precludes the use of many classic variance reduction techniques, e.g., subset simulation [62] and importance sampling [63].

To overcome this, a recently introduced scheme based on stratified sampling [64, 65] is adopted in the proposed framework. Basically, for wind sector n, the sample space of the wind speeds is partitioned into N_w mutually exclusive and collectively exhaustive subspaces (or strata), $E^{(n)}_{v_H,k}$. To ensure the collectively exhaustive nature of the partition, the lower bound wind speed of the first stratum is taken as zero whereas the last stratum is unbounded from above. With respect to the scheme used to identify the bounds of the individual stratum, leveraging how wind force is closely related to the square of the wind speed, a constant value is imposed for the difference between the square of the lower bound and upper bound wind speeds of each stratum. In other words, $E^{(n)}_{v_H,k} = [v^L_{H,k}, v^U_{H,k})$ for $k = 1, 2, ..., N_w$ where $v^L_{H,k}$ and $v^U_{H,k}$ are the lower and upper bound wind speeds defining the kth stratum under

the condition: $(v_{H,k}^L)^2 - (v_{H,k}^U)^2 = (v_{H,N_w}^L)^2/N_w$ for $k = 1, 2, ..., N_w - 1$. In addition, it is suggested to fix the lower bound of the last stratum, v_{H,N_w}^L, consistently with the order of magnitude of the failure probability expected in the simulation. Using the total probability theorem, the failure probability for sector n can then be estimated as:

$$P_{f_R}^{(n)} = \sum_{k=1}^{N_w} P_{f_R|E_{v_H,k}^{(n)}} P(E_{v_H,k}^{(n)}) \tag{12}$$

where N_w is the total number of strata; $P(E_{v_H,k}^{(n)})$ is the probability of v_H belonging to $E_{v_H,k}^{(n)}$ that can be directly estimated from the knowledge of the sector hazard curve $G_n(v_H)$; and $P_{f_R|E_{v_H,k}^{(n)}}$ is the probability of failure conditional on v_H belonging to $E_{v_H,k}^{(n)}$ that can be estimated using standard Monte Carlo (MC) methods as it is no longer a small failure probability.

As demonstrated in Arunachalam and Spence [64, 65], the COV of the estimator of $P_{f_R}^{(n)}$ can be written as:

$$\kappa_R^{(n)}(n_1, ..., n_{N_w}) = \frac{\sqrt{\sum_{k=1}^{N_w} \left[\left(P(E_{v_H,k}^{(n)}) \right)^2 P_{f_R|E_{v_H,k}^{(n)}} (1 - P_{f_R|E_{v_H,k}^{(n)}})/n_k \right]}}{\sum_{k=1}^{N_w} P(E_{v_H,k}^{(n)}) P_{f_R|E_{v_H,k}^{(n)}}} \tag{13}$$

where n_k is the number of samples in strata k. From the knowledge of $\kappa^{(n)}$, the following constrained optimization problem can be defined for finding the minimum stratum-wise allocation of samples for achieving target COVs on the failure probability estimates of N_R limit states:

$$\begin{aligned} &\text{Find} \qquad \{n_1, ..., n_{N_w}\} \\ &\text{to minimize} \qquad N_s = \sum_{k=1}^{N_w} n_k \\ &\text{s. t.} \quad \kappa_R^{(n)}(n_1, ..., n_{N_w}) \leq \tilde{\kappa}_R^{(n)} \quad \text{for} \quad R = 1, ..., N_R \end{aligned} \tag{14}$$

where N_s is the minimum number of samples while $\tilde{\kappa}_R^{(n)}$ for $R = 1, ..., N_R$ are the target COVs. It should be observed that the optimization problem of Eq. (14) requires a preliminary estimate of the conditional probabilities, $P_{f_R|E_{v_H,k}^{(n)}}$, which can be realized using MC simulation based on a limited set of equally allocated stratum samples [64, 65].

6. Case Study

6.1. Building Description

The proposed computational framework is illustrated on a 45-story archetype rectangular RC building located in New York City (NYC). This structural system was designed by the ASCE 7-22 Task Committee in support of the development of PBWE. The layout consists of a centrally placed concrete core wall system with coupling beams and fin walls providing lateral load-carrying resistance, as shown in Fig. 2 where the Y axis points north. The plan dimensions of the building are X = 45.72 m, Y = 30.48 m while the total height of the building is 180 m with a constant story height of 4 m. The building was designed using the current state of practice to satisfy the requirements of ASCE-22 [48] for a risk category II building. Equivalent static wind loads (ESWLs) corresponding to a 700-year return period winds were therefore used in the design. The ESWLs were provided by the wind tunnel consultant Cermak Peterka Petersen (CPP) while considering 2% modal damping and a site-specific climatological study. According to ASCE-22 [48], the target probability of failure for a risk category II building and limit states that are sudden and can result in widespread progression of damage is 3.5×10^{-6} (corresponding reliability index $\beta = 4.0$) over a 50-year lifespan. The nominal compressive strengths for the concrete composing the shear wall and coupling beams were 70 Mpa, 55 Mpa, and 40 Mpa for floors 1-18, 19-36, and 37-45 respectively. The reinforcing steel, both longitudinal and transverse, had a nominal yield stress of 420 MPa. It was assumed that the same steel batch was used for both the longitudinal and transverse reinforcing at each floor therefore resulting in a perfect correlation between F_y and f_{yh} at each floor. With respect to the gravity loads, the nominal dead load is defined by a self-weight of 4.8 kPa with a superimposed dead load of 0.72 kPa. The nominal reduced live load was 2 kPa.

6.2. Finite Element Model

The OpenSees finite element model of the building is shown in Fig. 3. The model was developed using sixteen MVLEM-3D elements at each floor. Displacement-based beam-column elements with five integration points and distributed plasticity were used to model the coupling beams. Each MVLEM-3D element considered 25 macro fibers while the rectangular

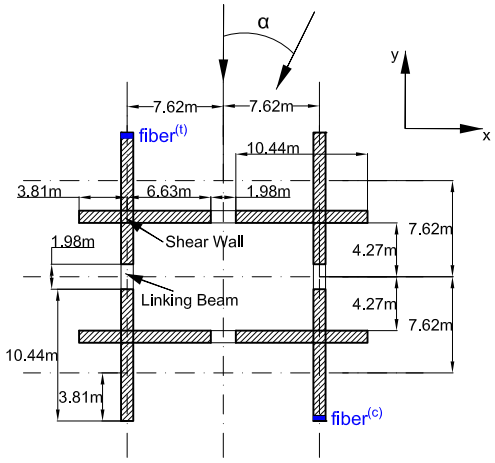

Figure 2: Planar layout of the archetype building.

coupling beams were discretized with 6 vertical fibers and 3 horizontal concrete fibers with steel fibers corresponding to the location of the reinforcing bars. The constitutive laws for the fibers corresponded to those discussed in Secs. 3.2.1 and 4 and denominated "Concrete02" and "SteelMPF" in OpenSees. The uncertain parameters of the constitutive laws were assigned consistently with Sec. 4.2.1 and 4.2.2. In particular, the concrete tensile strength was determined from the relationship $f_t = 0.31\sqrt{f'_c}$ [MPa] while the slope of the post-cracking model envelope in tension was taken as 5% [30]. The degree of confinement of the concrete of the core walls and coupling beams was considered by estimating K of Sec. 4.2.1 in terms of the transverse reinforcing of each component of the archetype building. For the reinforcing steel, the cyclic stiffness degradation characteristics were modeled using the parameter values suggested in [30] and therefore $\lambda = 0.1$.

6.3. Site-specific Wind Loads

6.3.1. Climatological Characterization

In implementing the sector-by-sector approach, the following eight sectors were considered: N, NE, E, SE, S, SW, W, and NW, as shown in Fig. 5. The largest sectorial mean annual wind speeds, v_H, were assumed to follow the same probability distribution as the non-directional wind speeds, $F_{V_H}^{(nd)}(v_H)$, which is described by a Type I distribution. To estimate $F_{V_H}^{(nd)}(v_H)$ and the subsequent wind hazard over the lifespan of the structure (i.e., 50 years as suggested in the ASCE 7-22), the annual site-specific 3 s gust wind speeds, v_3, correspond-

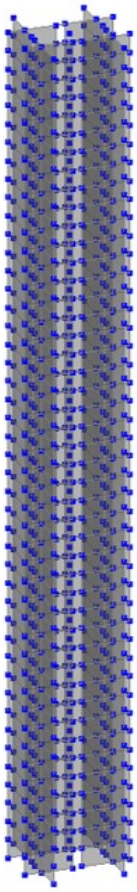

Figure 3: Opensees finite element model of the archetype building.

Table 5: Sectorial factors, κ_n, for NYC.

Sector	N	NE	E	SE	S	SW	W	NW
κ_n	0.88	0.88	0.84	0.84	0.84	0.88	1.00	0.92

ing to mean recurrence intervals (MRIs) of 700, 1700, 3000, 10,000, 100,000 and 1,000,000 years identified from the ASCE 7-22 hazard map [48] and transformed to $\bar{v}_H$ through the expression:

$$\bar{v}_H = \bar{b}\left(\frac{H}{10}\right)^{\bar{\alpha}} v_3 \tag{15}$$

where $\bar{b} = 0.47$ and $\bar{\alpha} = 1/4.5$ are the terrain exposure constants suggested by the ASCE 7-22 [48] for Exposure Category B. From the knowledge of $F_{V_H}^{(nd)}(v_H)$, the 50 year ($y = 50$) non-directional hazard curve can be estimated as: $G_{(y=50)}(v_H) = 1 - \left(F_{V_H}^{(nd)}(v_H)\right)^{50}$. As adopted in Chuang and Spence [19], the sectorial wind speeds were considered to be linearly related to the non-directional wind speeds through sectorial factors, κ_n, provided for NYC by CPP and reported in Table 5. It should be observed that, to account for the partial correlation of the sectoral wind speeds, these factors were intentionally increased by CPP to ensure at least one sector is characterized by non-directional wind speeds. The linear relationship between the non-directional and sectorial wind speeds allowed for the following definition of the sectorial CCDF of the lifespan maximum mean hourly wind speed: $G_n(v_H|n) = G_{(y=50)}(v_H/\kappa_n)$. The CCDF $G_n(\alpha|v_H)$ of wind direction conditional on v_H for sector n was taken as uniform.

Due to the linear relationship between the non-directional and directional wind speeds, the generation of samples from $G_n(v_H|n)$ can be achieved through directly sampling the stratified non-directional hazard curve, $G_{(y=50)}(v_H)$, of Fig. 4. The stratification was defined for this case study by considering the last stratum with the lower bound fixed by an annual exceedance probability of 1×10^{-7} (annual failure at which widespread progression of damage is expected for Risk Category II structures).

6.3.2. Aerodynamic Characterization

The POD-based stochastic wind load model of Sec. 3.3 was calibrated to building specific wind tunnel data collected on a 1:400 scale building model in urban surroundings by CPP.

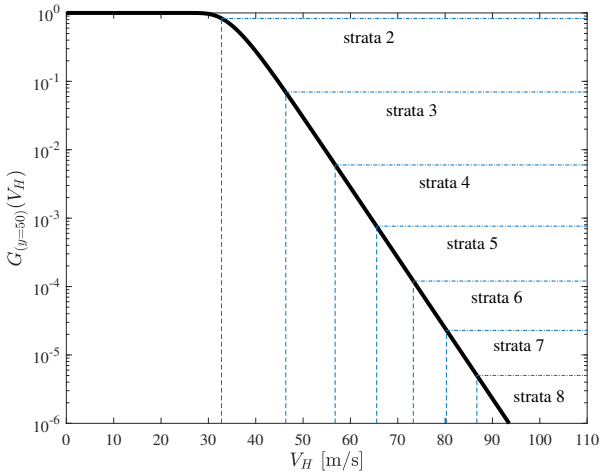

Figure 4: Site-specific stratified 50-year wind hazard curve.

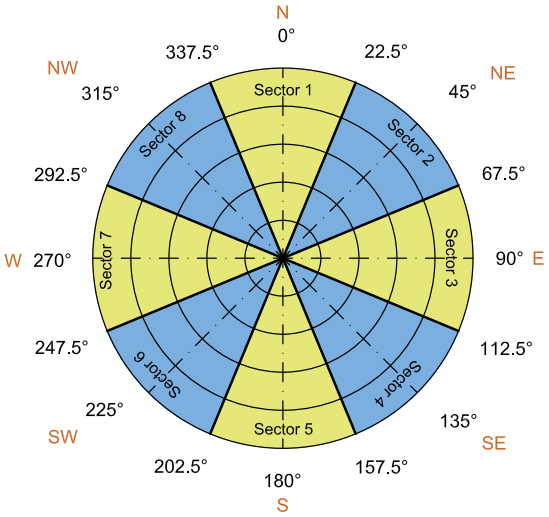

Figure 5: Wind direction sectors.

The test data were recorded for a sampling frequency of 250 Hz with a total duration of 81.92 s. The wind tunnel load histories, in terms of translational loads in X and Y directions as well as the torsional load around the vertical Z direction, were collected for 36 wind directions (i.e., $\alpha = 0°, 10°, ..., 350°$). These datasets were scaled using standard reduced frequency scaling and used to calibrate the stochastic wind load model. The first five POD modes were considered to this end as this has been demonstrated to be sufficient for representing the energy associated with the dynamic wind loads acting on high-rise buildings [66]. The total duration of the stochastic wind load samples was $T = 3660$ s with $T_a = 30$ s, $T_b = 3630$ s therefore leading to 3600 s of stationary wind loading. To directly estimate the residual structural behavior, an extra 45 s of zero loading was added to the end of each sample resulting in a total wind load duration of 3705 s. For a sample of v_H, α, and $\boldsymbol{y}_h$, the realizations of $\boldsymbol{f}(t; v_H, \alpha, \boldsymbol{y}_h)$ were generated with a full-scale sampling frequency of 0.1 s. However, based on the highest natural frequency of the system, the central difference scheme used to solve Eq. (4) required a time step of 0.000625 s or smaller. Therefore, the common practice of linear interpolation of the external excitation was carried out to reduce the sampling frequency of the external load to 0.000625 s.

6.4. Limit States Definition

The following suite of system and component-level limit states were considered consistently with what can be found in the literature [27, 11, 67];

- LS1: system collapse: maximum (over all floors) inter-story drift ratio exceeding $R = 1/20$ (5%);
- LS2-3: system displacement-based limit state 1: along-wind (LS2) and across-wind (LS3) maximum (over all floors) peak inter-story drift ratio exceeding $R = 1/50$;
- LS4-5: system displacement-based limit state 2: along-wind (LS4) and across-wind (LS5) maximum (over all floors) inter-story residual drift ratio exceeding $R = 1/1000$;
- LS6: compressive fiber experiencing concrete crushing/buckling of longitudinal reinforcing bars: compressive fiber strain exceeding $R = \epsilon_{20}$;
- LS7: tensile fracture of the reinforcing bars: tensile fiber strain exceeding $R = \epsilon_{sh}$.

6.5. Calibration of the Simulation Scheme

In implementing the sector-by-sector approach of Sec. 2.1, it is not generally necessary to solve Eq. (2) for all sectors. Indeed, it is common to use simplified elastic models of the system and key response parameters (e.g., peak base response moments) to identify the critical sectors [26, 25]. In this work, the critical sectors are identified by defining an elastic model of the system based on the initial tangent stiffness while considering the expected value of the random vector $\boldsymbol{y}_m$. The key response parameter was taken as the peak absolute resultant base moment, M_R, as this allows for the capture of the combined 3D response of the structure. To determine M_R, modal integration was used to rapidly solve the dynamic response of the system to realizations of $\boldsymbol{f}(t)$ calibrated as outlined in Sec. 6.3.2. Values of M_R were generated for each sector using the stratification of Fig. 4. For each sector, 3000 samples were considered with equal allocation between the stratum. The resulting CCDFs of M_R for a lifespan of 50 years are reported in Fig. 6 from which it is clearly seen that sector 7 (i.e., $\alpha \in [247.5^\circ - 292.5^\circ]$) is critical for the extreme response of the structure. Collapse simulation through the framework of this paper was therefore carried out in this sector.

To optimally allocate the samples for solving Eq. (2) among the strata of Sec. 6.3.1, a preliminary study with a total of 160 equally allocated samples (i.e., 20 samples per stratum) was first carried out. This enabled the preliminary estimation of $P_{f_R|E^{(n=7)}_{v_H,k}}$ from which the optimal stratum-wise sample allocation was identified for achieving a target COV of 20% on the probability of failure associated with the system-level limit states (i.e. LS1-LS5 of Sec. 6.4). This resulted in the requirement of an additional 773 samples to be allocated between the stratum as reported in Table 6.

6.6. Results

6.6.1. Reliability Assessment

The probabilities of failure, P_{f_R}, associated reliability indexes, β_{50}, as well as the corresponding COVs with respect to the limit states of Sec. 6.4 are reported in Table 7. In particular, LS6 and LS7 are associated with the critical compressive, fiber$^{(c)}$, and tensile, fiber$^{(t)}$, fibers of the system which are located at the base of the structure as illustrated in Fig. 2. From Table 7, it can be immediately seen that the structural system exceeds the

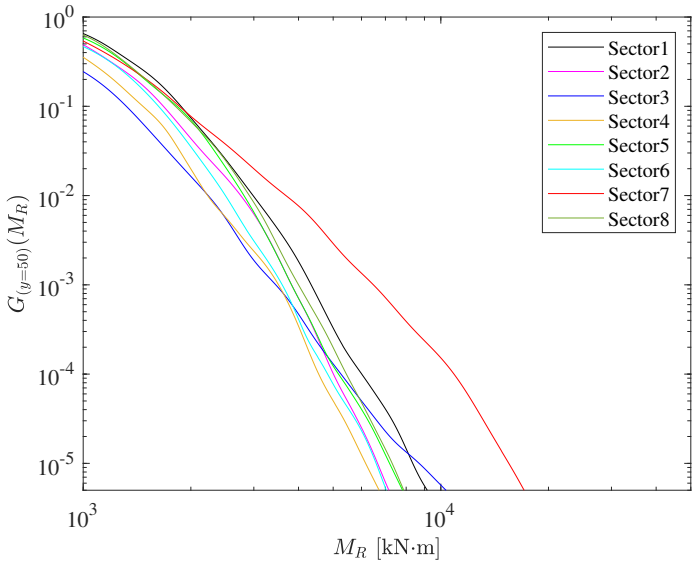

Figure 6: CCDFs of the resultant elastic base moment, M_R.

Table 6: Optimal sample allocation between the wind stratum.

Strata	$V_{H,k}^L$ (m/s)	$V_{H,k}^U$ (m/s)	Stratum samples
1	0.00	32.77	20
2	32.77	46.35	20
3	46.35	56.76	20
4	56.76	65.55	20
5	65.55	73.28	311
6	73.28	80.28	47
7	80.28	86.71	20
8	86.71	∞	475

target reliabilities reported in the ASCE 7-22 for a Risk Category II building. In particular, the component-level probability of concrete crushing/buckling of longitudinal reinforcing bars for the compressive fiber and reinforcing bar fracture for the tensile fiber exceed the target reliability of 4.0 by a significant margin illustrating the inherent inelastic capacity of the system against extreme winds. It is interesting to observe that the reliability index associated with peak inter-story drift ratio in the along-wind direction (LS2) is, for all intents and purposes, identical to the across-wind direction (LS3). This suggests that the along-wind and across-wind loads have a similar probability of resulting in extreme deformations. This is confirmed for the maximum inter-story residual drift ratio exceeding 1/1000 whose reliabilities are identical in the along-wind and across-wind directions.

Fig. 7 reports the empirical CCDFs of the maximum peak and residual inter-story drift ratios, D_r and $\hat{D}$ respectively. From Fig. 7, it is interesting to observe that, in terms of D_r, the limit of $R = 1/1000$ is critical. Indeed, once exceeded, residual deformations increase significantly in both the across-wind and along-wind directions with larger increases in the along-wind direction due to ratcheting. The exceedance of $R = 1/1000$ generally leads to collapse, as is evident from Table 7 where the reliability associated with LS1 is identical to that of LS4/5. With respect to $\hat{D}$, Fig. 7 shows how the across-wind response dominates until around $R = 1/50$ after which the along-wind response becomes dominant. This can be traced back to how initially, vortex shedding drives the peak response until the buffeting response causes enough ratcheting to exceed the across-wind response. Finally, it is interesting to observe from Fig. 7 how it is more likely for $\hat{D}$ to exceed $R = 1/50$, the collapse limit, in the along-wind direction rather than the across-wind direction, although both response directions contribute to the total exceedance probability of $R = 1/50$. The capability of the proposed framework to provide estimates of the CCDFs of the response parameters, as illustrated in Fig. 7, is extremely beneficial to the decision-making process as it provides information on the performance of the system over a full range of intensities and threshold values as opposed to estimating probabilities solely for a few predefined threshold values/limit states.

The capability of the stochastic simulation scheme of Sec. 5 to provide reliability estimates from extremely small sample sizes (total samples used was 933) for probabilities as small as 10^{-7} can be seen from the COVs of Table 7. Even though the target COVs of 20% were

Table 7: Failure probabilities and reliability indices over 50 years

Limit State	P_{f_R}	COV	β_{50}
LS1	4.37×10^{-7}	15.11%	4.92
LS2	5.90×10^{-7}	12.78%	4.86
LS3	3.39×10^{-7}	17.34%	4.97
LS4	4.37×10^{-7}	15.11%	4.92
LS5	4.37×10^{-7}	15.11%	4.92
LS6	1.09×10^{-7}	31.28%	5.18
LS7	4.37×10^{-8}	49.78%	5.35

not strictly met for the failure probabilities associated with LS1-LS5, reasonable COVs were still achieved. It is noteworthy that if simple MC simulation was used to estimate the failure probabilities with target COVs of 20%, approximately 250 million samples would be required. This clearly illustrates the efficiency of the stratified sampling scheme. The reason that the actual COVs differ from the target can be traced back to the fact the limited sample size of the preliminary study (20 samples per stratum) which can fail to provide adequate estimates of $P_{f_R|E^{(n)}_{v_H,k}}$. To strictly meet the target COVs, it would simply be necessary to solve the optimal sample allocation problem with the updated values of $P_{f_R|E^{(n)}_{v_H,k}}$. This would identify the strata where additional samples should be run to more accurately achieve the target COVs.

6.6.2. Collapse Mechanism Discussion

Samples that caused collapse, i.e., exceedance of LS1, occurred exclusively in the last wind speed stratum. In general, two typical collapse mechanisms were observed based on the deformed shape at the onset of collapse and the location of significant damage. These were: (1) flexure collapse at the base of the structure characterized by dominant along-wind deformation (denoted as Type-A collapse in the following); (2) collapse due to loss of horizontal load-bearing capacity at the base of the structure characterized by initiation through significant simultaneous along-wind and across-wind flexure (denoted as Type-B collapse in the following). Of the 475 samples generated in the last stratum, 27 led to

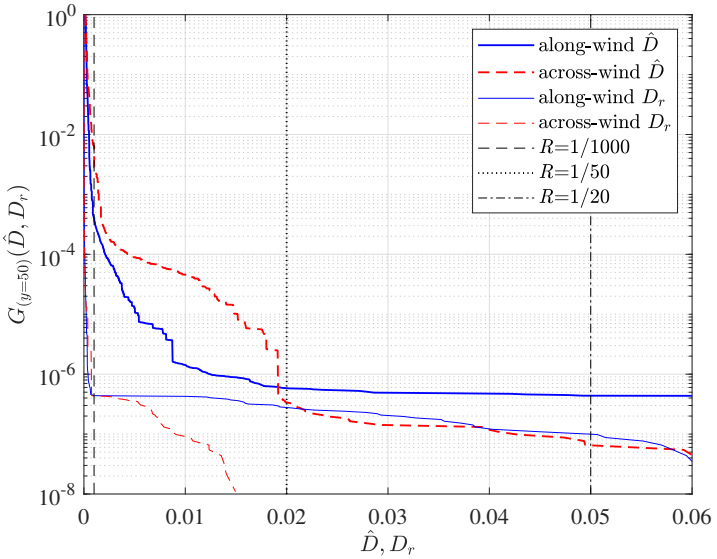

Figure 7: CCDFs of the maximum, over all floors, peak drift and residual drift ratios.

Type-A collapse while 13 led to Type-B collapse. The occurrence frequencies of the collapse mechanisms are therefore similar and generally characterized by severe damage towards the bottom of the structure (i.e., below $H/4$). This section will focus on the progression of component damage, and therefore the potential exceedance of LS6 and LS7, that ultimately led to the exceedance of LS1 and therefore the collapse of the structural system. It is important to note that in general several components must failure before collapse will occur, therefore the exceedance of LS6 and LS7 in a specific component does not necessarily imply collapse of the system.

Fig. 8 reports the X and Y roof displacements for the Type-A collapse sample. In particular, the sample was associated with a wind speed of $v_H = 104.96$ m/s and wind direction $\alpha = 280°$. As can be observed from Fig. 8, collapse occurs due to a sudden increase in the along-wind response which is caused by the collapse of the core walls at the base of the structure. The corresponding time histories of the base moments are reported in Fig. 9 from which it can be observed that no sudden change in loading caused the collapse, i.e., the collapse occurred due to a ratcheting type accumulation of damage. However, it can be seen that the initiation of component failure is caused by a significant along-wind moment at $T = 430$ s. As illustrated in Fig. 10 for the first floor, failure commences in the X-direction shear walls ($T = 430 - 1580$ s) with a predominance of damage in the downwind

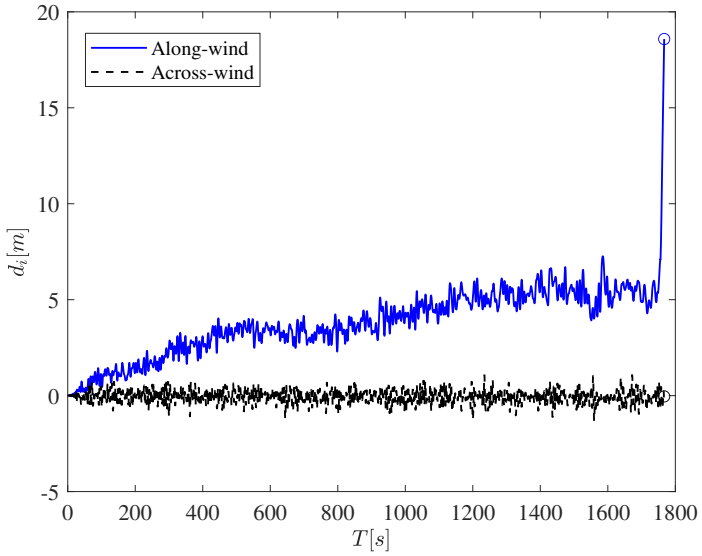

Figure 8: Type-A collapse sample ($v_H = 104.96$ m/s, $\alpha = 280°$): roof displacement time history response in X and Y direction.

walls. In particular, component failure is due to tensile fracture of the reinforcing bars in the upwind walls and LCF failure in the downwind walls. This progression of failure continues ($T = 1580 - 1754$ s) until concrete crushing and buckling of the reinforcing bars occurs in the downwind shear walls ($T = 1754 - 1766$ s) which ultimately leads to collapse. It is interesting to observe that this failure mechanism took over 20 minutes to develop illustrating how a ratcheting-type failure is present. It is worth noting that, although no substantial damage to the coupling beams occurred in this collapse sample, around half of the Type-A collapse samples did include significant damage to the X-direction coupling beams, with damage reaching as high as the 22nd floor.

Fig. 11 reports the X and Y roof displacements for the Type-B collapse sample which occurred for a wind speed of $v_H = 98.85$ m/s in direction $\alpha = 290°$. From Fig. 11, the sudden nature of the Type-B collapse mechanism is evident with the near simultaneous occurrence of large along-wind and across-wind responses. From Fig. 9, it is interesting to observe that, unlike the Type-A collapse mechanism, the initiation of collapse coincides with the simultaneous occurrence of significant along-wind and across-wind base moments, as highlighted by the base moments occurring at $T = 392$ s, i.e., time in which the collapse mechanism imitates. The critical floor for the representative Type-B collapse mechanism is

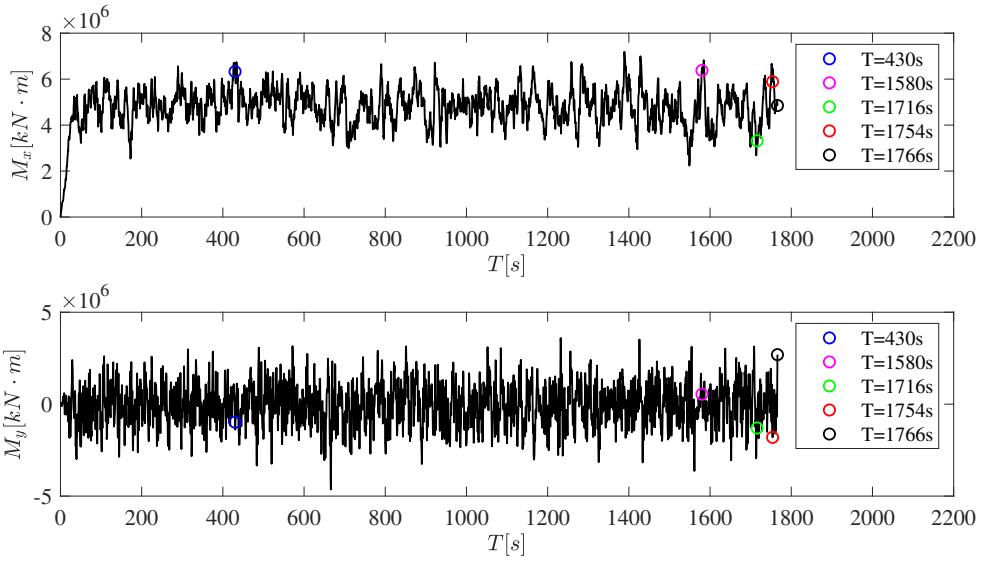

Figure 9: Type-A collapse sample ($v_H = 104.96$ m/s, $\alpha = 280°$): base moment time histories.

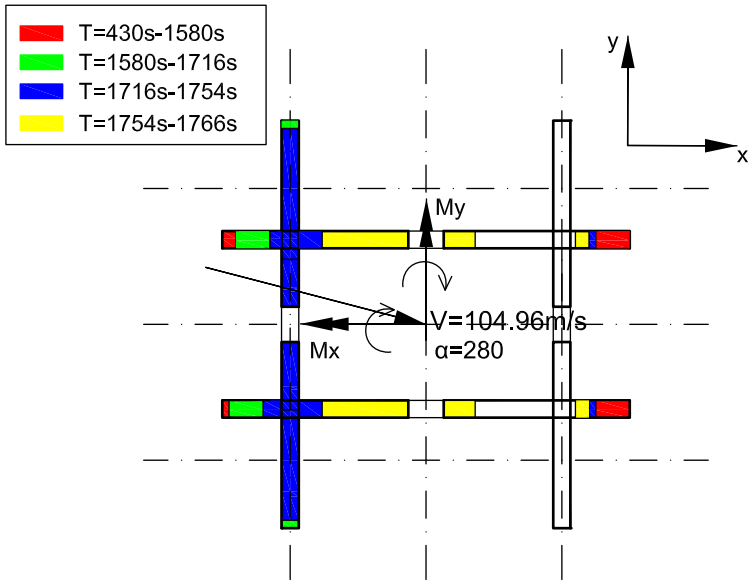

Figure 10: Type-A collapse sample ($v_H = 104.96$ m/s, $\alpha = 280°$): fiber failure progression at the critical (first) floor.

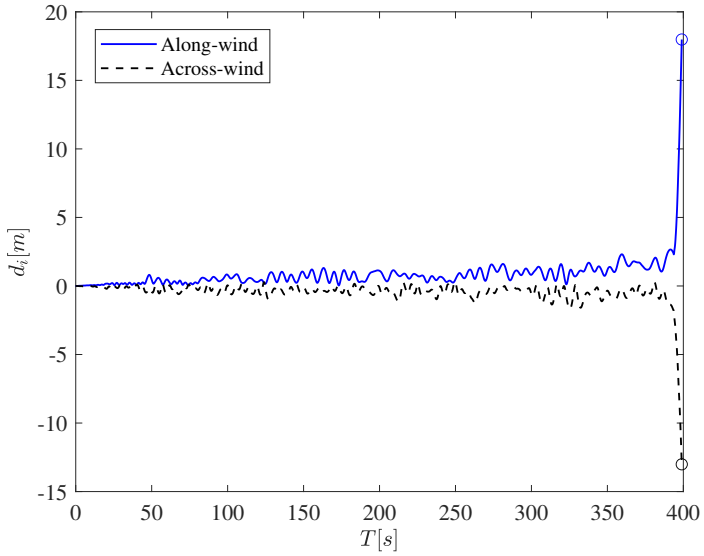

Figure 11: Type-B collapse sample ($v_H = 98.95$ m/s, $\alpha = 290°$): roof displacement time history response in X and Y direction.

the first floor. The failure progression at this floor is illustrated in Fig. 13. In particular, component collapse initiates in both the X- and Y-direction shear walls in the southeast corner of the structure. Failure is due to concrete crushing and buckling of the reinforcing bars. This failure mode rapidly evolves (over the time span of 2.6 seconds), including failure of the coupling beams at the base of the structure, until the entire system loses its vertical load-bearing capacity. It should be observed that while in this collapse sample vertical load-bearing capacity was ultimately lost leading to a pancake collapse of the structure, in around half of the observed Type-B collapse samples, the structure failed due to excessive lateral deformation without pancake effect.

As discussed above, the onset of collapse is closely aligned with component failure due to buckling of the reinforcing bars, concrete crushing, fatigue failure, and fracture of the reinforcing bars. Fig. 14 reports the stress-strain hysteretic curves for select fibers experiencing such failure. In particular, Fig. 14a illustrates the case of fiber failure due to concrete crushing with reinforcing bar buckling, which is the predominant fiber failure mode for the Type-B failure mechanism. More in detail, when the compressive strain of the macro fiber reaches the concrete crushing strain limit, the "MinMax" model drops the stress and stiffness of the fiber to zero with respect to both concrete and reinforcing bar materials. Fig. 14b illustrates

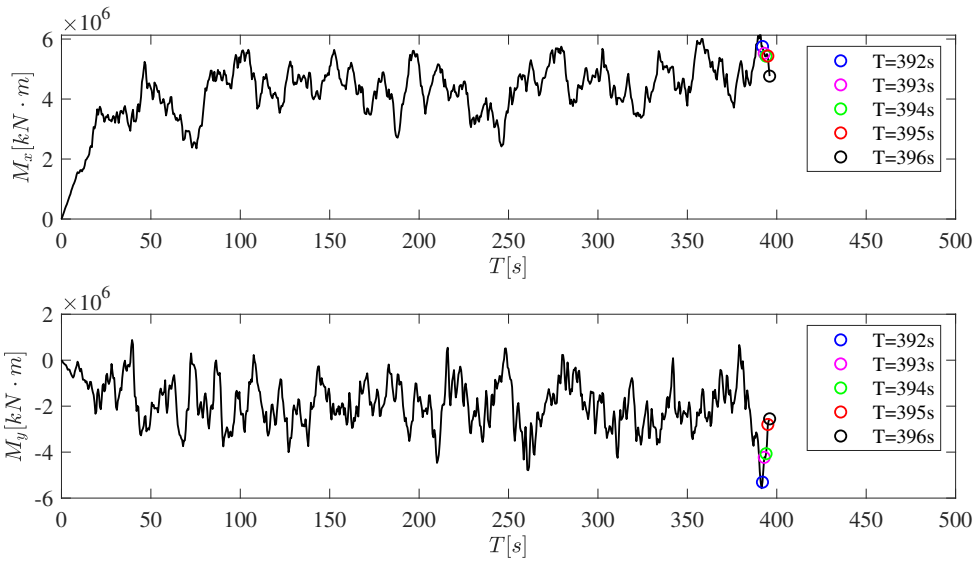

Figure 12: Type-B collapse sample ($v_H = 98.85$ m/s, $\alpha = 290°$): base moment time histories.

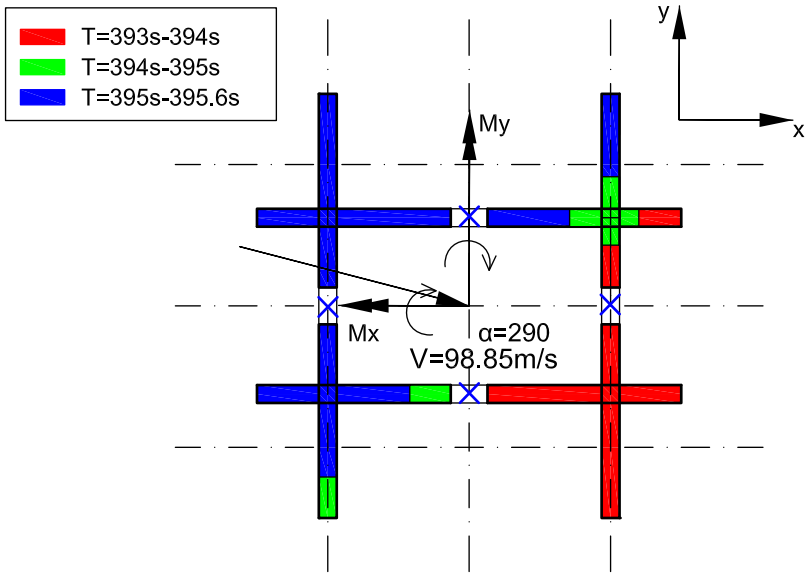

Figure 13: Type-B collapse sample ($v_H = 98.85$ m/s, $\alpha = 290°$): fiber failure progression at the critical (first) floor.

failure due to concrete cracking in tension followed by reinforcing bar fracture which is the predominant fiber failure mode for the Type-A failure mechanism. When the macro fiber is in tension, the concrete quickly cracks, with stress and stiffness dropping to zero. The reinforcing bars continue to resist the tension forces until they eventually fail due to fracture from excessive tensile strain. Fig. 14c illustrates fiber failure due to LCF under cyclic loads that cause concrete fiber failure in tension due to cracking (seen in the representative Type-A failure mechanism).

7. Conclusions

This work introduced a general framework for the reliability-based collapse assessment of reinforced concrete structures subject to extreme winds. The framework was based on modeling the response of the structure in a fiber-based finite element environment that incorporated the use of 3D macro fiber elements for the explicit modeling of shear walls as well as schemes for the capture of low cycle fatigue failure, fracture and buckling of the reinforcing bars together with crashing failure and cyclic degradation of the concrete. The dynamic wind loads were modeled through a stochastic scheme calibrated to building specific wind tunnel data therefore enabling the capture of both record-to-record variability (path-dependent effects) as well as any complex aerodynamic features seen in the wind tunnel. To efficiently propagate uncertainty and estimate the small failure probabilities that generally characterize the collapse of code-compliant buildings, the framework was integrated with a recently introduced stratified sampling scheme that enables the simultaneous estimation of failure probabilities (or reliabilities) associated with multiple limit states of interest. The framework was illustrated on the collapse analysis of a 45-story archetype reinforced concrete structure with a hypothetical location in New York City. From the results, the capability of the framework to provide estimates of small failure probabilities associated with the extreme response of the structure was seen with failure probabilities as small as 10^{-7} estimated with coefficients of variation of around 20% using less than 1000 samples. In terms of the observed performance of the archetype structure, collapse reliabilities were seen to significantly exceed the target values of the archetype design highlighting the significant inelastic capacity of reinforced concrete structures. When collapse did occur, two mechanisms were observed with

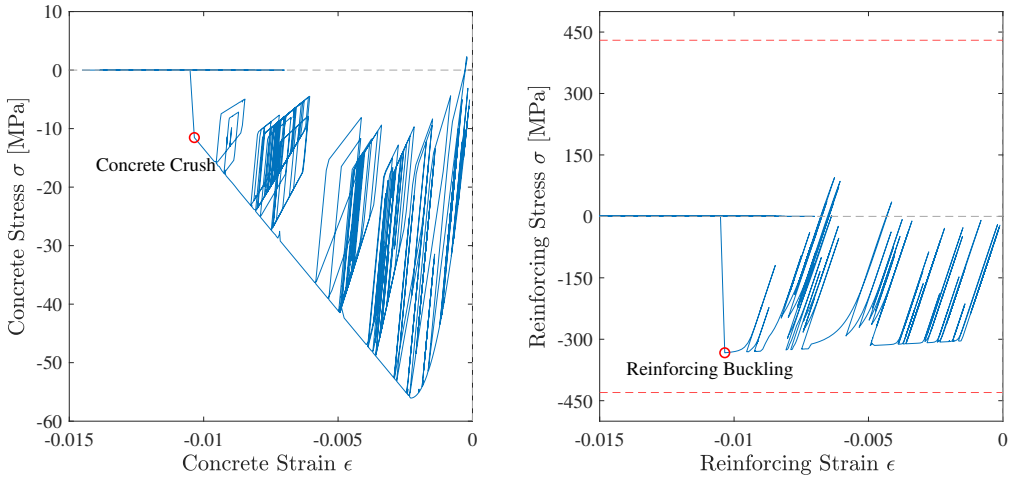

(a)

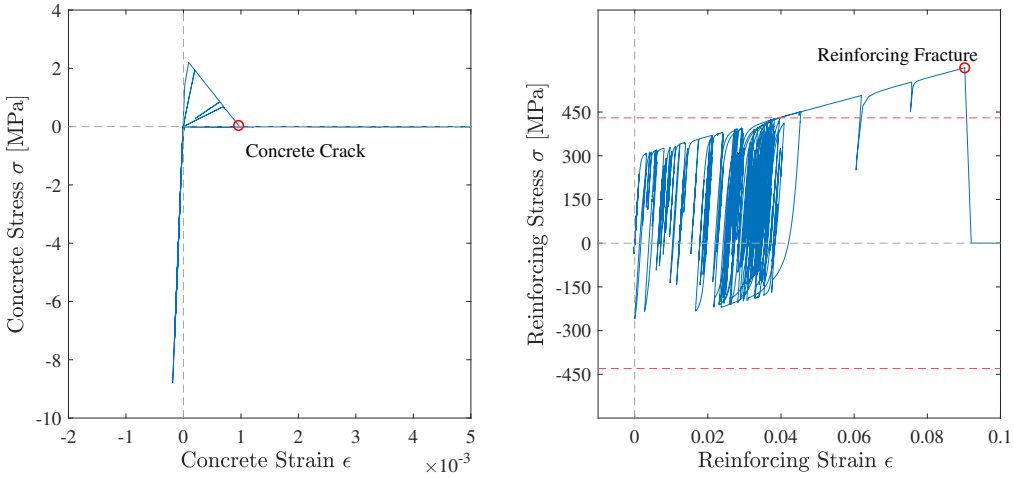

(b)

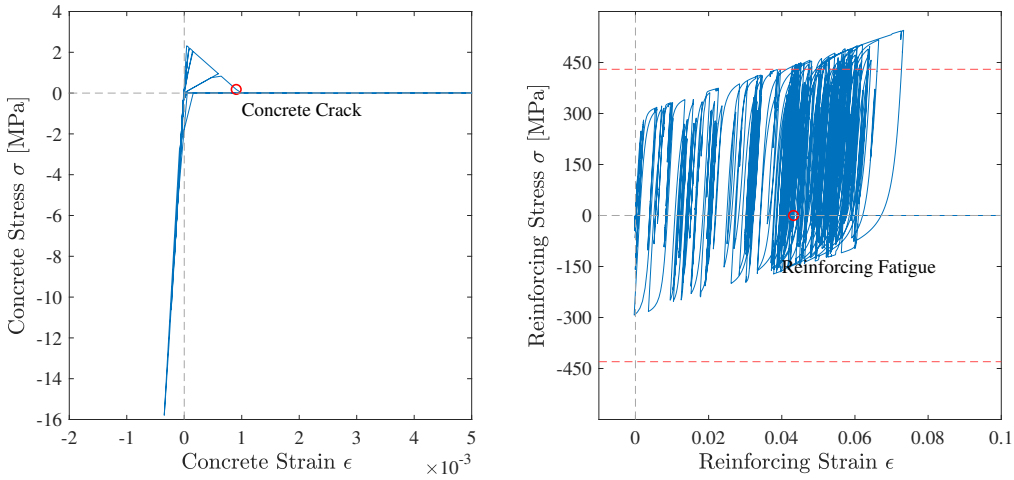

(c)

Figure 14: Representative stress-strain curves for the fiber failure modes: (a) concrete crushing/reinforcing bar buckling failure mode; (b) reinforcing bar fracture failure mode; (c) reinforcing bar fatigue failure mode.

both involving significant interaction between along-wind and across-wind response. In the first mechanism, damage accumulated over a relatively long period of time ($\approx$ 20 minutes) while in the second, damage occurred rapidly ($\approx$ 3 seconds) and led, in some cases, to a complete loss of vertical load bearing capacity. The failure mechanisms were characterized by concrete crushing/buckling of the reinforcing, reinforcing fatigue failure, and reinforcing fracture illustrating the complexity of wind-induced collapse. It is believed that the proposed framework and the insight gained on the extreme behavior of wind-excited reinforced concrete structures can be of use to the further development of performance-based wind engineering.

Acknowledgments

This research effort was supported in part by the National Science Foundation (NSF) under Grant No. CMMI-2118488. This support is gratefully acknowledged.

References

[1] Spence, S.M.J., Arunachalam, S.. Performance-based wind engineering: Background and state of the art. Frontiers in Built Environment 2022;26:830207.

[2] Jain, A., Srinivasan, M., Hart, G.C.. Performance based design extreme wind loads on a tall building. The Structural Design of Tall Buildings 2001;10(1):9–26.

[3] Ciampoli, M., Petrini, F., Augusti, G.. Performance-based wind engineering: towards a general procedure. Structural Safety 2011;33(6):367–378.

[4] Beck, A.T., Kougioumtzoglou, I.A., dos Santos, K.R.M.. Optimal performance-based design of non-linear stochastic dynamical RC structures subject to stationary wind excitation. Engineering Structures 2014;78:145–153.

[5] Spence, S.M.J., Kareem, A.. Performance-based design and optimization of uncertain wind-excited dynamic building systems. Engineering Structures 2014;78:133–144.

[6] Ouyang, Z., Spence, S.M.J.. A performance-based wind engineering framework for envelope systems of engineered buildings subject to directional wind and rain hazards. Journal of Structural Engineering 2020;146(5):04020049.

[7] Petrini, F., Francioli, M.. Next generation PBWE: Extension of the SAC-FEMA method to high-rise buildings under wind hazards. Structural Safety 2022;99:102255.

[8] Abdelwahab, M., Ghazal, T., Nadeem, K., Aboshosha, H., Elshaer, A.. Performance-based wind design for tall buildings: Review and comparative study. Journal of Building Engineering 2023;68:106103.

[9] Porter, K.A.. An overview of peer's performance-based earthquake engineering methodology. In: Proceedings of ninth international conference on applications of statistics and probability in civil engineering. 2003, p. 1–8.

[10] Pacific Earthquake Engineering Research Center, . Guidelines for performance-based seismic design of tall buildings. Tech. Rep.; Pacific Earthquake Engineering Research Center; University of California, Berkeley; 2010.

[11] American Society of Civil Engineers, . Prestandard for performance-based wind design. American Society of Civil Engineers; 2019,.

[12] Judd, J.P., Charney, F.A.. Inelastic behavior and collapse risk for buildings subjected to wind loads. In: Structures Congress 2015. 2015, p. 2483–2496.

[13] Feng, C., Chen, X.. Crosswind response of tall buildings with nonlinear aerodynamic damping and hysteretic restoring force character. Journal of Wind Engineering and Industrial Aerodynamics 2017;167:62–74.

[14] Feng, C., Chen, X.. Inelastic responses of wind-excited tall buildings: Improved estimation and understanding by statistical linearization approaches. Engineering structures 2018;159:141–154.

[15] Huang, J., Chen, X.. Uncertainty analysis of inelastic response of high-rise buildings to wind using a reduced-order building model. Engineering Structures 2023;288:116224.

[16] Chuang, W.C., Spence, S.M.J.. A performance-based design framework for the integrated collapse and non-collapse assessment of wind excited buildings. Engineering Structures 2017;150:746–758.

[17] Chuang, W.C., Spence, S.M.J.. An efficient framework for the inelastic performance assessment of structural systems subject to stochastic wind loads. Engineering Structures 2019;179:92–105.

[18] Chuang, W.C., Spence, S.M.J.. Probabilistic performance assessment of inelastic wind excited structures within the setting of distributed plasticity. Structural Safety 2020;84:101923.

[19] Chuang, W.C., Spence, S.M.J.. A framework for the efficient reliability assessment of inelastic wind excited structures at dynamic shakedown. Journal of Wind Engineering and Industrial Aerodynamics 2022;220:104834.

[20] Arunachalam, S., Spence, S.M.J.. Reliability-based collapse assessment of wind-excited steel structures within performance-based wind engineering. Journal of Structural Engineering 2022;148(9):04022132.

[21] Zheng, X.W., Li, H.N., Gardoni, P.. Hybrid bayesian-copula-based risk assessment for tall buildings subject to wind loads considering various uncertainties. Reliability Engineering & System Safety 2023;233:109100.

[22] Zuniga, M.M., Murangira, A., Perdrizet, T.. Structural reliability assessment through surrogate based importance sampling with dimension reduction. Reliability Engineering & System Safety 2021;207:107289.

[23] Xu, Z., Wang, H., Xing, C., Tao, T., Mao, J., Liu, Y.. Physics guided wavelet convolutional neural network for wind-induced vibration modeling with application to structural dynamic reliability analysis. Engineering Structures 2023;297:117027.

[24] Nguyen, P.T., Manuel, L.. Uncertainty quantification in low-probability response estimation using sliced inverse regression and polynomial chaos expansion. Reliability Engineering & System Safety 2024;242:109750.

[25] Isyumov, N., Ho, E., Case, P.. Influence of wind directionality on wind loads and responses. Journal of Wind Engineering and Industrial Aerodynamics 2014;133:169–180.

[26] Irwin, P., Garber, J., Ho, E.. Integration of wind tunnel data with full scale wind climate. In: Proceedings of the 10th Americas Conference on Wind Engineering. 2005, p. 132–135.

[27] Lu, X., Tian, Y., Sun, C., Zhang, S.. Development and application of a high-performance triangular shell element and an explicit algorithm in opensees for strongly nonlinear analysis. CMES-Comp Model Eng Sci 2019;120:561–582.

[28] Mazzoni, S., McKenna, F., Scott, M.H., Fenves, G.L.. OpenSees command language manual. Berkeley, California, United States; 2006.

[29] Beyer, K., Dazio, A., Priestley, M.J.N.. Inelastic wide-column models for u-shaped reinforced concrete walls. Journal of Earthquake Engineering 2008;12(S1):1–33.

[30] Kolozvari, K., Kalbasi, K., Orakcal, K., Wallace, J.. Three-dimensional model for nonlinear analysis of slender flanged reinforced concrete walls. Engineering Structures 2021;236:112105.

[31] Terzic, V., Kolozvari, K.. Evaluation of post-earthquake functional recovery for a 42-story building located in los angeles. In: Proceedings of 2020 Los Angeles Tall Buildings Structural Design Council Annual Conference. 2020, p. 93–113.

[32] Kolozvari, K., Kalbasi, K., Orakcal, K., Wallace, J.. Three-dimensional shear-flexure interaction model for analysis of non-planar reinforced concrete walls. Journal of Building Engineering 2021;44:102946.

[33] Denavit, M.D., Hajjar, J.F.. Description of geometric nonlinearity for beam-column analysis in opensees 2013;.

[34] Orakcal, K.. Nonlinear modeling and analysis of slender reinforced concrete walls. University of California, Los Angeles; 2004.

[35] Yassin, M.H.M.. Nonlinear analysis of prestressed concrete structures under monotonic and cyclic loads. University of California, Berkeley; 1994.

[36] Kent, D.C., Park, R.. Flexural members with confined concrete. Journal of the Structural Division 1971;97(7):1969–1990.

[37] Scott, B.D., Park, R., Priestley, M.J.N.. Stress-strain behavior of concrete confined by overlapping hoops at low and high strain rates. Journal of the American Concrete Institute, 1982;97(7):13–27.

[38] Menegotto, M.. Method of analysis for cyclically loaded rc plane frames including changes in geometry and non-elastic behavior of elements under combined normal force and bending. In: Proc. of IABSE symposium on resistance and ultimate deformability of structures acted on by well defined repeated loads. 1973, p. 15–22.

[39] Filippou, F.C., Popov, E.P., Bertero, V.V.. Effects of bond deterioration on hysteretic behavior of reinforced concrete joints 1983;.

[40] Uriz, P.. Towards earthquake resistant design of concentrically braced steel structures. University of California, Berkeley; 2005.

[41] Ballio, G., Castiglioni, C.A.. A unified approach for the design of steel structures under low and/or high cycle fatigue. Journal of Constructional Steel Research 1995;34(1):75–101.

[42] Charney, F.A.. Unintended consequences of modeling damping in structures. Journal of Structural Engineering 2008;134(4):581–592.

[43] Chopra, A.K., McKenna, F.. Modeling viscous damping in nonlinear response history analysis of buildings for earthquake excitation. Earthquake Engineering & Structural Dynamics 2016;45(2):193–211.

[44] Judd, J.P.. Windstorm resilience of a 10-story steel frame office building. ASCE-ASME Journal of Risk and Uncertainty in Engineering Systems, Part A: Civil Engineering 2018;4(3):04018020.

[45] Chen, X., Kareem, A.. Proper orthogonal decomposition-based modeling, analysis, and simulation of dynamic wind load effects on structures. Journal of Engineering Mechanics 2005;131(4):325–339.

[46] Suksuwan, A., Spence, S.M.J.. Optimization of uncertain structures subject to stochastic wind loads under system-level first excursion constraints: a data-driven approach. Computers & Structures 2018;210:58–68.

[47] Duarte, T.G.A., Arunachalam, S., Subgranon, A., Spence, S.M.J.. Uncertainty quantification and simulation of wind-tunnel-informed stochastic wind loads. Wind 2023;3(3):375–393.

[48] American Society of Civil Engineers, . Minimum design loads and associated criteria for buildings and other structures. American Society of Civil Engineers; 2022,.

[49] Kiureghian, A.D.. Non-ergodicity and peer's framework formula. Earthquake engineering & structural dynamics 2005;34(13):1643–1652.

[50] Nowak, A.S., Rakoczy, A.M., Szeliga, E.K.. Revised statistical resistance models for R/C structural components. Special Publication 2012;284:1–16.

[51] Barbato, M., Gu, Q., Conte, J.P.. Probabilistic push-over analysis of structural and soil-structure systems. Journal of Structural Engineering 2010;136(11):1330–1341.

[52] Tubaldi, E., Barbato, M., Dall'Asta, A.. Influence of model parameter uncertainty on seismic transverse response and vulnerability of steel–concrete composite bridges with dual load path. Journal of Structural Engineering 2012;138(3):363–374.

[53] Haukaas, T., Scott, M.H.. Shape sensitivities in the reliability analysis of nonlinear frame structures. Computers and Structures 2006;84:964–977.

[54] Karamanci, E., Lignos, D.G.. Computational approach for collapse assessment of concentrically braced frames in seismic regions. Journal of Structural Engineering 2014;140(8):A4014019.

[55] Lu, X., Lu, X., Guan, H., Ye, L.. Collapse simulation of reinforced concrete high-rise building induced by extreme earthquakes. Earthquake Engineering & Structural Dynamics 2013;42(5):705–723.

[56] Sadek, F., Diniz, S., Kasperski, M., Gioffrè, M., Simiu, E.. Sampling errors in the estimation of peak wind-induced internal forces in low-rise structures. Journal of engineering mechanics 2004;130(2):235–239.

[57] Bernardini, E., Spence, S.M.J., Kwon, D.K., Kareem, A.. Performance-based design of high-rise buildings for occupant comfort. Journal of Structural Engineering 2015;141(10):04014244.

[58] Diniz, S.M.C., Simiu, E.. Probabilistic descriptions of wind effects and wind-load factors for database-assisted design. Journal of Structural Engineering 2005;131(3):507–516.

[59] Zhang, H., Ellingwood, B.R., Rasmussen, K.J.R.. System reliabilities in steel structural frame design by inelastic analysis. Engineering structures 2014;81:341–348.

[60] Galambos, T.V., Ellingwood, B., MacGregor, J.G., Cornell, C.A.. Probability based load criteria: Assessment of current design practice. Journal of the Structural Division 1982;108(5):959–977.

[61] Ellingwood, B.. Development of a probability based load criterion for American National Standard A58: Building code requirements for minimum design loads in buildings and other structures; vol. 577. Department of Commerce, National Bureau of Standards; 1980.

[62] Au, S.K., Beck, J.L.. Estimation of small failure probabilities in high dimensions by subset simulation. Probabilistic engineering mechanics 2001;16(4):263–277.

[63] Melchers, R.E.. Importance sampling in structural systems. Structural Safety 1989;6(1):3–10.

[64] Arunachalam, S., Spence, S.M.J.. An efficient stratified sampling scheme for the simultaneous estimation of small failure probabilities in wind engineering applications. Structural Safety 2023;101:102310.

[65] Arunachalam, S., Spence, S.M.J.. Generalized stratified sampling for efficient reliability assessment of structures against natural hazards. Journal of Engineering Mechanics 2023;149:04023042.

[66] Suksuwan, A., Spence, S.M.J.. Performance-based design optimization of uncertain wind excited systems under system-level loss constraints. Structural Safety 2019;80:13–31.

[67] Zaker Esteghamati, M., Banazadeh, M., Huang, Q.. The effect of design drift limit on the seismic performance of rc dual high-rise buildings. The Structural Design of Tall and Special Buildings 2018;27(8):e1464.